

6. ANTARCTICA—S. Stammerjohn, Ed.

a. Overview—S. Stammerjohn

In strong contrast to 2014, 2015 was marked by low regional variability in both atmospheric and oceanic anomalies, at least for the first half of the year. The Antarctic-wide distribution of anomalies coincided with a strong positive southern annular mode (SAM) index. However, by October; the high-latitude response to El Niño became evident, but the associated anomalies were rather atypical compared to the mean response from six previous El Niño events. Simultaneously, a somewhat tardy but unusually large and persistent Antarctic ozone hole developed. These springtime conditions imparted strong regional contrasts late in the year, particularly in the West Antarctic sector. Other noteworthy Antarctic climate events from 2015 are below:

- For most of the year surface pressure was lower and temperatures were cooler than the 1981–2010 climatology, along with stronger-than-normal circumpolar westerly winds, slightly higher-than-normal precipitation over the ocean areas, and mostly shorter-than-normal melt seasons on the continent. These anomalies were consistent with the positive SAM index registered in all months except October. February had a record high SAM index value of +4.92 (13% higher than the previous high value recorded over 1981–2010).
- There was an abrupt but short-lived switch in the mean surface temperature anomaly for the continent (from cold to warm) and a weakening of the negative surface pressure anomaly in October 2015. These atmospheric circulation changes coincided with the emerging high-latitude response to El Niño, the ozone hole, and a shift in the SAM index from positive to negative.
- The 2015 Antarctic ozone hole was amongst the largest in areal coverage and most persistent, based on the record of ground and satellite observations starting in the 1970s. This very large ozone hole was caused by unusually weak stratospheric wave dynamics, resulting in a colder- and stronger-than-normal stratospheric polar vortex. The persistently below-normal temperatures enabled larger ozone depletion by human-produced chlorine and bromine compounds, which are still at fairly high levels despite their continuing decline resulting from the Montreal Protocol and its Amendments.
- Although the 2015 El Niño produced strong atmospheric circulation anomalies in the South Pacific, thus affecting temperatures and sea ice

in the West Antarctic sector, its impact across the rest of Antarctica was weaker due to an atypical teleconnection pattern.

- There was a continuation of near-record high Antarctic sea ice extent and area for the first half of 2015, with 65 sea ice extent and 46 sea ice area daily records attained by July. However, at mid-year, there was a reversal of the sea ice anomalies, shifting from record high levels in May to record low levels in August. This was then followed by a period of near-average circumpolar sea ice (relative to the 36-year satellite record).
- Together with unusually high sea ice extent, particularly in the West Antarctic sector, SSTs were also cooler than average, in contrast to warmer-than-normal SSTs equatorward of the polar front. South of the polar front, sea surface height anomalies were negative, consistent with the mostly positive SAM index. Compared to 2014, there was a small decrease in sea level detected around the continental margin as well, leading to a slight increase in the estimated volume transport of the Antarctic Circumpolar Current. These changes are, however, superimposed on longer-term increases in sea level and a potential small decrease in volume transport. The 2015 deep ocean observations at 140°E indicate a continued freshening of Antarctic Bottom Water, relative to observations in the late 1960s and more frequent observations since the 1980s.

Details on the state of Antarctica's climate in 2015 and other climate-related aspects of the Antarctic region are provided below, starting with the atmospheric circulation, surface observations on the continent (including precipitation and seasonal

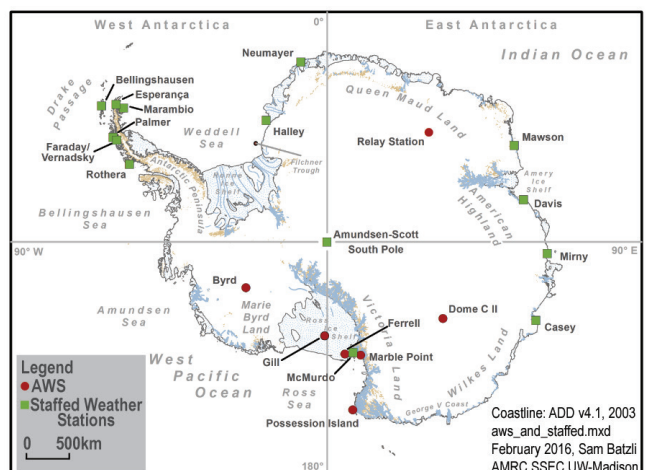


FIG. 6.1. Map of stations and other regions used throughout the chapter.

melt), ocean observations (including sea ice and ocean circulation), and finally the Antarctic ozone hole. Newly included this year is the southern high latitude response to El Niño (Sidebar 6.1) and the state of Antarctic ecosystems in the face of climate perturbations (Sidebar 6.2). Place names used in this chapter are provided in Fig. 6.1.

b. Atmospheric circulation—K. R. Clem, S. Barreira, and R. L. Fogt

The 2015 atmospheric anomalies across Antarctica were dominated by below-average surface temperatures over much of coastal and interior Antarctica from January to September, particularly across the Antarctic Peninsula and the surrounding Weddell and Bellingshausen Seas. Negative pressure anomalies in the Antarctic troposphere during the first half of the year weakened in August, while the stratosphere poleward of 60°S became very active beginning in June with strong negative pressure and temperature anomalies and an amplification of the stratospheric vortex. Using a station-based SAM index (normalized difference in zonal mean sea level pressure between 40°S and 65°S; Marshall 2003), the generally low pressure conditions gave rise to positive SAM index values, which were observed in every month except October during 2015. Figure 6.2 depicts a vertical cross section of the geopotential height anomalies (Fig. 6.2a) and temperature anomalies (Fig. 6.2b) averaged over the polar cap (60°–90°S), as well as the circumpolar zonal wind anomalies (Fig. 6.2c) averaged over 50°–70°S and the Marshall (2003) SAM index average for each month.

Climatologically, the year was split into four time periods (denoted by vertical red lines in Fig. 6.2) that were selected based on periods of similar temperature and pressure anomalies (Fig. 6.3). The composite anomalies (contours) and standard deviations (from the 1981–2010 climatological average; shading) for each of the time periods are shown in Fig. 6.3; surface pressure anomalies are displayed in the left column and 2-m temperature anomalies in the right column.

During January–March, the large-scale circulation was marked with negative geopotential height (Fig. 6.2a) and surface pressure (Fig. 6.3a) anomalies over Antarctica and positive surface pressure anomalies over much of the middle latitudes. The Marshall SAM index was strongly positive, and reached a record monthly mean high value during February [+4.92; Fig. 6.2; Marshall (2003); SAM index values start in 1957]. At this time, the circumpolar zonal winds exceeded 2 m s⁻¹ (>1.5 standard deviations) above the climatological average throughout the

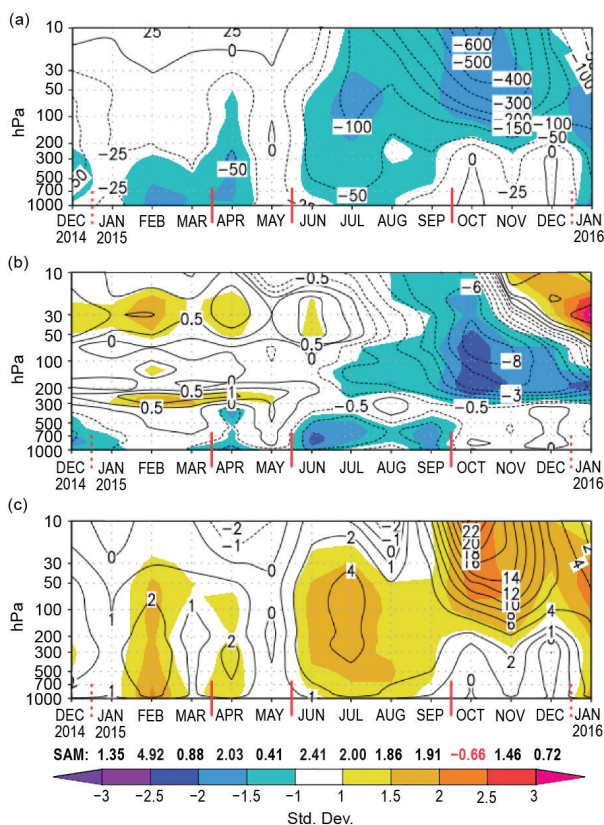


FIG. 6.2. Area-weighted averaged climate parameter anomalies for the southern polar region in 2015 relative to 1981–2010: (a) polar cap (60°–90°S) averaged geopotential height anomalies (contour interval is 50 m up to ±200 m with additional contour at ±25 m, and 100 m contour interval after ±200 m); (b) polar cap averaged temperature anomalies (contour interval is 1°C up to ±4°C with additional contour at ±0.5°C, and 2°C contour interval after ±4°C); (c) circumpolar (50°–70°S) averaged zonal wind anomalies (contour interval is 2 m s⁻¹ with additional contour at ±1 m s⁻¹). Shading represents standard deviation of anomalies from the 1981–2010 climatological average. (Source: ERA-Interim reanalysis.) Red vertical bars indicate the four separate climate periods used for compositing in Fig. 6.2; the dashed lines near Dec 2014 and Dec 2015 indicate circulation anomalies wrapping around the calendar year. Values from the Marshall (2003) SAM index are shown below panel (c) in black (positive values) and red (negative values).

troposphere and lower stratosphere (Fig. 6.2c). Much of the coastal Antarctic 2-m temperatures were below average (Fig. 6.3b), with the exception of areas of the Ross Ice Shelf and Wilkes Land (~90°E–180°). Positive temperature anomalies were observed throughout much of the stratosphere over the polar cap (Fig. 6.2b).

Positive SAM index values continued during April but weakened in May. This was due to a strong positive surface pressure anomaly southwest of Australia, while the remainder of the middle latitudes experi-

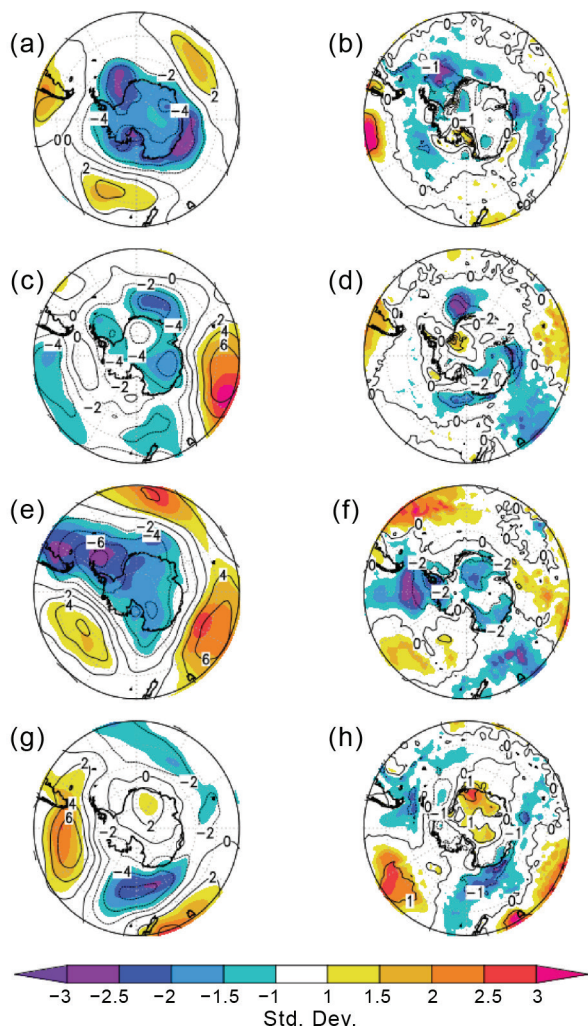


FIG. 6.3. (left) Surface pressure anomalies and (right) 2-m temperature anomalies relative to 1981–2010 for (a) and (b) Jan–Mar 2015; (c) and (d) Apr–May 2015; (e) and (f) Jun–Sep 2015; and (g) and (h) Oct–Dec 2015. Contour interval for (a), (c), (e), and (g) is 2 hPa; contour interval for (b) and (h) is 1°C and contour interval for (d) and (f) contour interval is 2°C. Shading represents standard deviations of anomalies relative to the selected season from the 1981–2010 average. (Source: ERA-Interim reanalysis.)

enced negative surface pressure anomalies with a weakening of the circumpolar zonal winds in May (Fig. 6.2c). Much of East Antarctica was colder than average, particularly offshore along coastal Queen Maud Land (30°W–0°) and portions of the Ross Sea westward towards Mirny station (~90°E), while the Amundsen Sea and the Ronne-Filchner Ice Shelf were slightly warmer than average (Fig. 6.3d).

During June–September, negative polar-cap averaged geopotential height anomalies and positive circumpolar zonal wind anomalies were observed

throughout the troposphere and stratosphere. Strong positive surface pressure anomalies occurred over the South Pacific, southwest of Australia, and over the South Atlantic, while strong negative surface pressure anomalies occurred over the Weddell Sea (Fig. 6.3e); these conditions led to positive SAM index values through September. Antarctic 2-m temperatures were primarily below average (Fig. 6.3f), with anomalies over the Antarctic Peninsula, Bellingshausen Sea, and eastern Amundsen Sea more than 2.5 standard deviations below the climatological average.

By October–December, positive surface pressure and 2-m temperature anomalies developed over interior East Antarctica, with the strongest warming noted over Queen Maud Land, while the Drake Passage and coastal Wilkes Land remained colder than average (Figs. 6.3g,h). A strong negative surface pressure anomaly was observed south of New Zealand and a strong positive surface pressure anomaly was observed in the southeastern South Pacific, likely tied to the strengthening of the El Niño conditions in the tropical Pacific. These circulation anomalies over the South Pacific brought cold, southerly flow to the coastal and offshore regions of Wilkes Land and the offshore region of the northwestern Antarctic Peninsula, respectively. Meanwhile, the stratosphere over the polar cap became very active after September. Negative temperature and geopotential height anomalies of 1–2 standard deviations below the climatological average propagated down through the stratosphere from October to December. A marked strengthening of the stratospheric circumpolar vortex occurred in response to the stratospheric cooling, with positive zonal wind anomalies exceeding 1–2 standard deviations above the climatological average throughout the stratosphere to finish the year. Over this time period (October–December) the SAM index values also weakened, and a negative value was observed in October 2015, coincident with the weaker and more regional nature of the near-surface conditions (Fig. 6.3).

c. Surface manned and automatic weather station observations—S. Colwell, L. M. Keller, M. A. Lazzara, A. Setzer, R. L. Fogt, and T. Scambos

The circulation anomalies described in section 6b are discussed here in terms of observations at staffed and automatic weather stations (AWS). Climate data that depict regional conditions are displayed for four staffed stations (Bellingshausen on the Antarctic Peninsula, Halley in the Weddell Sea, Mawson in the Indian Ocean sector, and Amundsen-Scott at the South Pole; Figs. 6.4a–d) and two AWSs (Byrd in West

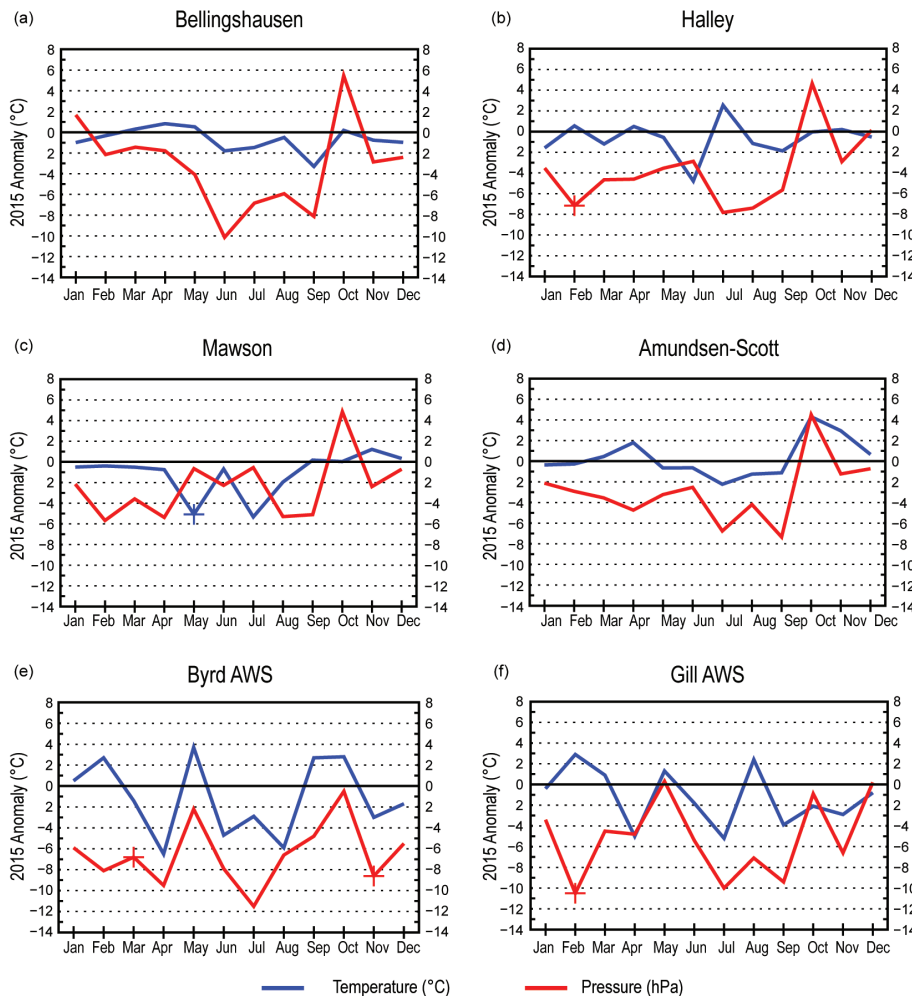


FIG. 6.4. 2015 Antarctic climate anomalies at six representative stations [four staffed (a)–(d) and two automatic (e)–(f)]. Monthly mean anomalies for temperature (°C) and surface pressure (hPa) are shown, with + denoting record anomalies for a given month at each station in 2015. All anomalies are based on differences from 1981–2010 averages, except for Gill, which is based on averages during 1985–2013. Observational data start in 1968 for Bellingshausen, 1957 for Halley and Amundsen-Scott, 1954 for Mawson, 1985 for Gill AWS, and 1981 for Byrd AWS.

Antarctica and Gill on the Ross Ice Shelf; Figs. 6.4e,f). To better understand the statistical significance of records and anomalies discussed in this section, references can be made to the spatial anomaly maps in Fig. 6.3 (the shading indicates the number of standard deviations the anomalies are from the mean).

Monthly mean temperatures at Bellingshausen station (Fig. 6.4a) on the western side of the Antarctic Peninsula were similar to the 1981–2010 mean at the start and end of the year, but from May to September, the values were consistently lower than the mean. Midway down on the west side of the Antarctic Peninsula, the temperatures at Rothera (not shown) followed a similar pattern. In the Weddell Sea region, the monthly mean temperatures at Halley (Fig. 6.4b) and Neumayer (not shown) were within $\pm 2^{\circ}\text{C}$ of the

1981–2010 mean, with the exception of June and July at Halley. In June, the mean monthly value nearly matched the lowest recorded mean monthly value and included a new record for the extreme daily minimum value, which was -56.2°C . The anomalously cold conditions in June were followed by a respite to anomalously warm conditions in July that were then followed by below- to near-average temperatures for the rest of the year.

Around the coast of East Antarctica, all of the Australian stations had near-average temperatures at the start and end of the year and colder-than-average temperatures from April to August, except for Casey (not shown) in June when the temperature was slightly higher than average. Davis (not shown) and Mawson (Fig. 6.4c) both had very low monthly mean temperatures in

May (a record low at Mawson). Temperatures at Mawson were also anomalously low again in July. At Amundsen-Scott station (Fig. 6.4d), the monthly mean temperatures were close to the long-term means with the exception of October and November when they were warmer than average.

In the Antarctic Peninsula, an all-time record warm air temperature for the continent may have been set at Esperança on 24 March, reaching $+17.5^{\circ}\text{C}$ during an intense foehn wind event that spanned much of the northeastern Peninsula. Temperatures rose as much as 30°C within 48 hours as an intense high pressure region over the Drake Passage and strong low pressure over the northwestern Weddell Sea drove strong downslope winds all along eastern Graham Land. An automated sensor at Foyn Point in

the Larsen B embayment recorded still higher values briefly, at +18.7°C on the 24th, and several other weather stations in the region surpassed +17°C on 23 and 24 March.

Temperatures at the AWS locations provide a broader view of weather records and trends for the continent. For the Ross sector, Possession Island (not shown) reported a record low temperature of -21.9°C (greater than 2 standard deviations from the 1981–2010 mean) in September and then tied its record high mean temperature of 1.7°C in December. Otherwise, temperatures at Possession Island were above normal for February, August, October, November, and December and below normal for the rest of the months (no report for July). The Ross Ice Shelf region (e.g., Gill AWS, Fig. 6.4f) had generally above-normal temperatures from January through March and again in August, but these warm periods were interspersed by colder-than-normal temperatures, especially in April, July, and September. In West Antarctica, Byrd AWS (Fig. 6.4e) was colder than normal for March–April, June–August, and November–December and was warmer than normal otherwise. At Relay Station (not shown) on the Polar Plateau, temperatures were above normal through May, below normal for June–September, and then 5°C above normal in October. On the other side of the Polar Plateau, Dome C II (not shown) did not operate from May through part of September, but October and November had above-normal temperatures.

While stations over Antarctica generally did not report record temperature anomalies, many staffed and unstaffed stations reported record low pressure anomalies in at least one month. The pressure data from all staffed stations showed lower-than-average pressures for all months except October (Figs. 6.4a–d) and January at the Bellingshausen station (Fig. 6.4a). On the Ross Ice Shelf, almost every month had below-normal pressure with a record low anomaly reported for February for Possession Island (-6.7 hPa), Marble Point (-9.2 hPa, greater than 2 standard deviations below normal), Ferrell (-9.9 hPa, about 2 standard deviations below normal), and Gill AWS (-10.5 hPa, greater than 2 standard deviations below normal; the latter shown in Fig. 6.4f). The record low pressure anomalies ranged from -6.7 to -10.5 hPa. Possession Island was only above normal for May, and Marble Point had slightly above-normal pressure for October. Relay Station also had a record low pressure anomaly in February (-5.1 hPa), and pressures were below normal through the whole year until October. The record low pressure anomalies observed in February on both the Ross Ice Shelf and at Relay Station also coincided

with the record high SAM index value (Fig. 6.2c). Byrd AWS (Fig. 6.4e) in West Antarctica reported record low pressures in March and November (803.7 and 799.8 hPa, respectively), with only four other months reporting pressure anomalies less than 6 hPa below normal. There were also a few reported wind speed records (not shown), but most stations generally reported only slightly above or below normal wind speeds over the course of the year. Marble Point had a record low monthly mean wind speed of 2.4 m s⁻¹ in March, and Gill reported a record low wind speed of 1.5 m s⁻¹ in April (both more than 2 standard deviations below normal). Relay Station had a record high monthly mean wind speed of 9.1 m s⁻¹ in April (greater than 2 standard deviations above normal).

d. Net precipitation (P–E)—D. H. Bromwich and S.-H. Wang

Precipitation minus evaporation/sublimation ($P - E$) closely approximates the surface mass balance over Antarctica, except for the steep coastal slopes (e.g., Bromwich et al. 2011; Lenaerts and van den Broeke 2012). Precipitation variability is the dominant term for $P - E$ changes at regional and larger scales over the Antarctic continent. There are few precipitation gauge measurements for Antarctica, and those are compromised by blowing snow. In addition, over the interior Antarctic plateau, snowfall amounts are often less than the minimum gauge resolution. As a result, precipitation and evaporation fields from the Japanese 55-year Reanalysis (JRA-55; Kobayashi et al. 2015) were examined to assess Antarctic net precipitation ($P - E$) behavior for 2015. JRA-55, the second generation of JRA, is produced with a low-resolution version of the Japan Meteorological Agency's (JMA) operational data assimilation system as of December 2009, which incorporated many improvements achieved since JRA-25 (Onogi et al. 2007), including a revised longwave radiation scheme, four-dimensional data assimilation, bias correction for satellite radiances, and assimilation of newly available homogenized observations. These improvements have resulted in better fits to observations, reduced analysis increments and improved forecast results (Kobayashi et al. 2015). The model is run at a spatial resolution of TL319 (~0.5625° or 55 km) and at 60 vertical levels from the surface up to 0.1 hPa. In comparison to other long-term global reanalyses (e.g., NCEP1 and NCEP2), JRA has higher horizontal and vertical model resolution, uses a greater number of observations, and has a more advanced model configuration (e.g., Bromwich et al. 2007; Kang and Ahn 2015).

Figure 6.5 shows the JRA-55 2015 and 2014 annual anomalies of $P - E$ and mean sea level pressure

(MSLP) departures from the 1981–2010 average. In general, annual $P - E$ anomalies (Figs. 6.5a,b) over the high interior of the continent are small (within $\pm 50 \text{ mm yr}^{-1}$), but larger anomalies can be observed along the coast, consistent with the low and high snow accumulation in these regions. At higher latitudes ($> 60^\circ\text{S}$) JRA-55 is quantitatively similar to JRA-25 and ERA-I (European Centre for Medium-Range Weather Forecasts Interim reanalysis) $P - E$ results (Bromwich and Wang 2014, 2015). The excessively high positive anomalies of JRA-25 over the Southern Ocean north of 60°S (that were noted in last year's report) are not present in JRA-55. JRA-55 also shows better overall agreement with ERA-I than JRA-25 during 2013 and 2014.

Based on JRA-55, the 2014 negative anomalies located at eastern Queen Maud Land (between 15° and 80°E) are weaker in 2015, and positive anomalies are observed over Enderby Land and the Amery Ice Shelf. The strong negative features between American Highland and Wilkes Land (between 80° and 150°E) observed in 2014 were replaced by weak positive anomalies in 2015, except near the Budd Coast region (near 115°E) where negative anomalies were observed again. The George V Coast and Ross Sea had positive anomalies in 2015, in contrast to 2014 conditions. The small positive anomalies over the western Ross Sea seen in 2014 were replaced by negative anomalies in 2015. Strong positive anomalies over the Amundsen and Bellingshausen Seas (between 150° and 75°W) in 2014 were weaker but remained positive in 2015. Small negative anomaly centers were present along

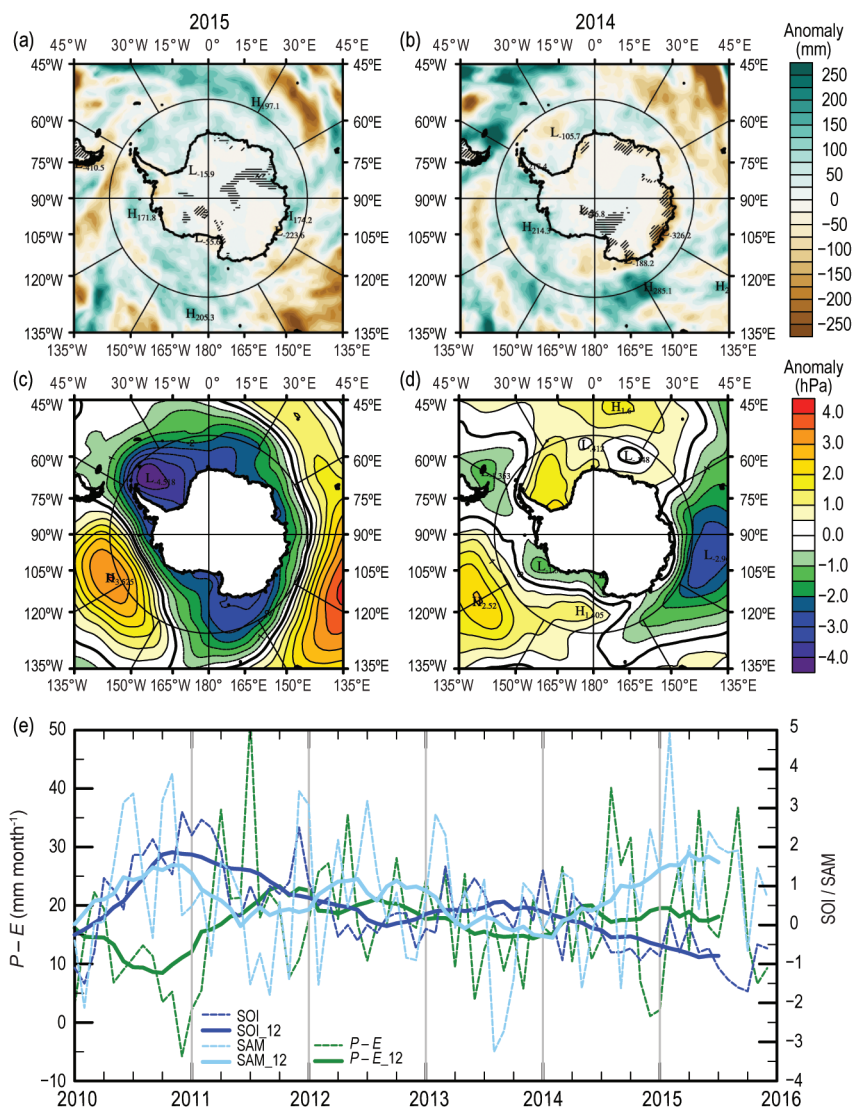


FIG. 6.5. JRA-55 (a–d) annual $P - E$ and MSLP anomalies: (a) 2015 $P - E$ anomalies (mm month^{-1}); (b) 2014 $P - E$ anomalies (mm month^{-1}); (c) 2015 MSLP anomalies (hPa); and (d) 2014 MSLP anomalies (hPa). All anomalies are departures from the 1981–2010 mean. (e) Monthly total $P - E$ (mm ; dashed green) for the West Antarctic sector bounded by $75^\circ - 90^\circ\text{S}$, $120^\circ\text{W} - 180^\circ$, along with the SOI (dashed dark blue, from NOAA Climate Prediction Center) and SAM [dashed light blue, from Marshall (2003)] indices since 2010. In (a) and (b), Antarctic regions with greater than $\pm 30\%$ change are hatched; sloping denotes negative values and horizontal denotes positive. Centered annual running means are plotted as solid lines.

the West Antarctic coastline in 2015. Both sides of the Antarctic Peninsula have similar anomaly patterns to 2014, but were weaker. The negative $P - E$ anomaly center over the Weddell Sea in 2014 was replaced by a positive one in 2015.

These annual $P - E$ anomaly features were generally consistent with the mean atmospheric circulation implied by the MSLP anomalies (Figs. 6.5c,d). In 2015 the MSLP anomalies surrounding Antarctica were less localized than in 2014 (Figs. 6.5c,d). The MSLP

pattern in 2015 consisted of large negative pressure anomalies over Antarctica (or high latitudes) and a ring of positive pressure anomalies at midlatitudes, which resulted in positive SAM index values recorded for most of 2015 (Figs. 6.2c, 6.5e). This MSLP pattern tended to induce higher precipitation from the Southern Ocean into Antarctica. The positive MSLP anomaly over the Ronne Ice Shelf and the Weddell Sea in 2014 was replaced by a strong negative anomaly center at the tip of the Antarctic Peninsula in 2015. Enhanced cyclonic flows induced more inflow from the ocean and resulted in higher precipitation anomalies into the Weddell Sea and Queen Maud Land. A strong negative anomaly center at the southern Indian Ocean (near 105°E) in 2014 was replaced by large positive anomalies, with weak negative anomalies along the coast of East Antarctica. Combined with cyclonic flow produced by negative anomalies over Weddell Sea, it produced higher precipitation along Queen Mary Coast (between 60° and 125°E) in 2015. The large positive anomaly center in 2014 over the South Pacific Ocean (near 120°W) was enhanced in 2015. In combination with the expanded and strengthened negative anomalies over the western Ross Sea region, above-normal precipitation was observed in the Ross Sea and Amundsen Sea regions (Fig. 6.5a).

Earlier studies show that almost half of the moisture transport into Antarctica occurs in the West Antarctic sector. Here, there is also large interannual variability in moisture transport in response to atmospheric circulation patterns associated with extreme ENSO events (e.g., Bromwich et al. 2004) and high SAM index values (e.g., Fogt et al. 2011). As the seasons progressed from 2014 to 2015, the negative MSLP anomalies over the Ross Sea weakened (Figs. 6.3a,c, 6.5d), while a positive MSLP anomaly deepened offshore of 60°S (Figs. 6.5c,d). A positive anomaly then appeared in the Bellingshausen Sea and strengthened in later months of 2015 (Figs. 6.3e,g). These anomaly features are consistent with a simultaneously strong El Niño event and a positive SAM index. Figure 6.5e shows the time series of average monthly total $P - E$ over Marie Byrd Land–Ross Ice Shelf (75°–90°S, 120°W–180°) and the monthly Southern Oscillation index (SOI) and SAM indices (with 12-month running means). It is clear that the SOI and SAM index were

positively associated with each other, but negatively associated with $P - E$, in most months from 2010 to mid-2011. From then on, the SOI and SAM index were negatively associated through 2015. From 2014 into 2015, the SOI became more negative (indicating El Niño conditions in the tropical Pacific), while the SAM index became more positive. The atmospheric circulation pattern associated with a positive SAM index modulated the high latitude response to El Niño, and the associated MSLP anomalies were located farther north than normal (Sidebar 6.1). The end result was near-normal precipitation over Marie Byrd Land–Ross Ice Shelf (Fig. 6.5e), in contrast to higher-than-normal precipitation during previous El Niño events (e.g., Bromwich et al. 2004).

e. Seasonal melt extent and duration—L. Wang and H. Liu

Seasonal surface melt on the Antarctic continent during 2014/15 was estimated from daily measurements of passive microwave brightness temperature using data acquired by the Special Sensor Microwave–Imager Sounder (SSMIS) onboard the Defense Meteorological Satellite Program (DMSP) *F17* satellite. The data were preprocessed and provided by the U.S. National Snow and Ice Data Center (NSIDC) in level-3 EASE-Grid format (Armstrong et al. 1994) and were analyzed using a wavelet transform-based edge

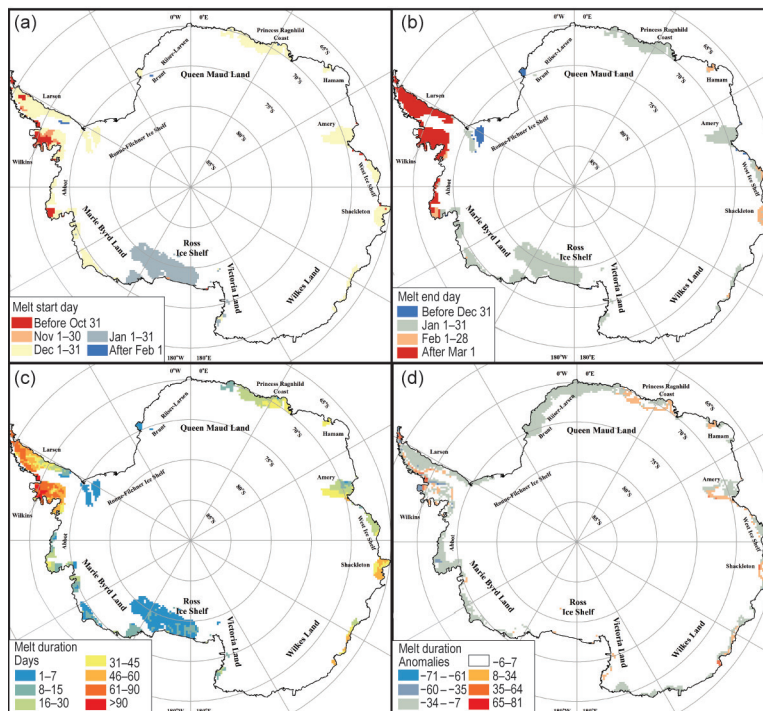


FIG. 6.6. Estimated surface melt for the 2014/15 austral summer (a) melt start day, (b) melt end day, (c) melt duration (days), and (d) melt duration anomalies (days) relative to 1981–2010. (Data source: DMSP SSMIS daily brightness temperature observations.)

During 2015, a strong El Niño developed and intensified in the tropical Pacific. Like much of the globe, Antarctica is influenced during ENSO events by a series of atmospheric Rossby waves emanating from the tropical Pacific, extending to high latitudes over the South Pacific Ocean near West Antarctica (Turner 2004). This pattern has been widely referred to as the Pacific South American pattern, and during an El Niño event, positive pressure anomalies are typical off the coast of West Antarctica (Mo and Ghil 1987; Karoly 1989).

Despite the 2015/16 El Niño’s emergence as a strong event in the Pacific by midyear, its impact near Antarctica was not at all typical. However, true to form, in September–December (SOND) 2015, the high-latitude South Pacific was marked by a strong positive pressure anomaly and associated counterclockwise near-surface flow (Figs. SB6.1a, 6.3g). The southerly flow in the vicinity of the Antarctic Peninsula partially explains the persistence of below-average temperatures across the Antarctic Peninsula in the latter half of 2015 (compare Figs. 6.3f,h with Fig. 6.4a). Elsewhere, the pattern of response was quite different from recent strong El Niño events (Fig. SB6.1b). The southern Pacific positive pressure anomaly, although much stronger than the El Niño average, was displaced northward. While this had consistent temperature and wind impacts across the Antarctic Peninsula and the South Pacific, much of the rest of West Antarctica was not strongly impacted in 2015 as is typical during other strong El Niño events (compare Fig. SB6.1b with Fig. 6.3e,g and Byrd AWS data in Fig. 6.4e). The northward displacement of the high pressure anomaly in 2015 is most likely due to the fact that much of 2015, with the exception of October, was marked by a positive SAM index (compare Fig. 6.2c). Because the SAM index monitors the strength and/or position of the circumpolar jet, which is known to influence extratropical Rossby wave propagation and breaking (L’Heureux and Thompson 2006; Fogt et al. 2011; Gong et al. 2010, 2013), the strengthened jet in 2015 was not so favorable for Rossby wave propagation into the higher (>60°) southern latitudes. Thus, the South Pacific teleconnection was displaced farther north than normal (based on Fig. SB6.1b). Historically, many of the strongest El Niño events occurred during negative SAM index values

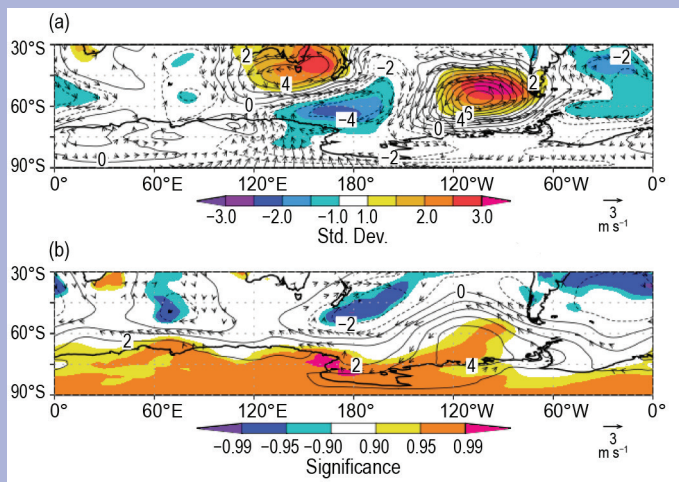


FIG. SB6.1. (a) SOND MSLP (contoured) and 10-m wind anomalies (vectors) from the 1981–2010 climatological mean. Shading represents the number of standard deviations the 2015 SOND MSLP anomalies were from the climatological mean; wind vectors are only shown if at least one component was a standard deviation outside the climatological mean. (b) MSLP (contoured) and 10-m wind (vectors) anomaly composite for the six strongest El Niño events in SOND since 1979 (in rank order: 1997, 1982, 1987, 2002, 2009, 1991), with shading (from lightest to darkest shades) indicating composite mean anomalies (of MSLP and winds) significantly different from zero at $p < 0.10$, $p < 0.05$, $p < 0.01$, respectively, based on a two-tailed Student’s *t* test. The shading therefore indicates where the El Niño composite mean is significantly different from the 1981–2010 climatology. (Source: ERA-Interim reanalysis.)

(Fogt et al. 2011) in contrast to the 2015 El Niño event. Nonetheless, because of its influence on meridional flow over the ice edge at the time of maximum sea ice extent (Figs. SB6.1a, 6.8c), the end of 2015 was marked by strong regional sea ice extent anomalies in the West Antarctic sector (Figs. 6.8c,d, 6.9c–e), which were opposite in sign to the long-term trends in sea ice extent in that region (Fig. 6.8e).

In summary, the 2015 El Niño indeed produced strong atmospheric circulation impacts in the South Pacific, which are consistent with the below-average temperatures across the Antarctic Peninsula and sea ice extent anomalies in the Bellingshausen, Amundsen, and Ross Seas. However, because the teleconnection was displaced farther north than normal, its impact across the rest of Antarctica was much weaker than was the case for previous strong El Niño events.

detection method (Liu et al. 2005). The algorithm delineates each melt event in the time series by tracking its onset and end dates, with the onset day of the first melt event being the start day of the melt season (Fig. 6.6a) and the end day of the last melt event being the end day of the melt season (Fig. 6.6b). The melt duration is then the total number of melting days per pixel during the defined melt season (excluding any refreezing events that may have occurred during this period; Fig. 6.6c). The melt extent and melt index are metrics useful for quantifying the interannual variability in surface melt (Zwally and Fiegles 1994; Liu et al. 2006). Melt extent (km^2) is the total area that experienced surface melt for at least one day, while the melt index ($\text{day}\cdot\text{km}^2$) is the product of duration and melt extent and describes the spatiotemporal variability of surface melting. The anomaly map (Fig. 6.6d) was created by referencing the mean melt duration computed over 1981–2010 (see also Fig. 3 in Liu et al. 2006).

The spatial pattern of the melt duration map in austral summer 2014/15 (Fig. 6.6c) was similar to previous years (Wang et al. 2014). Areas with extended melt duration (>45 day duration in orange-red) were the Antarctic Peninsula area, including the Larsen and Wilkins ice shelves, and parts of coastal East Antarctica, including the Shackleton ice shelf and other smaller ice shelves east of there. Areas with moderate melt duration (16–45 day duration in green-yellow) included much of coastal Queen Maud Land and the Amery, West, and Abbot ice shelves; short-term melt (<16 day duration in blues) occurred on the coast of Marie Byrd Land, including Ross ice shelf and portions of Queen Maud Land near the Filchner Ice Shelf.

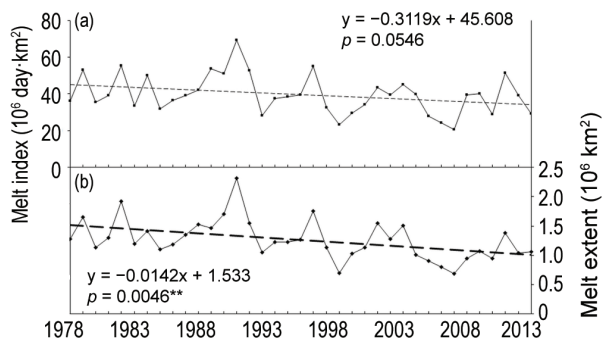


FIG. 6.7. (a) Melt index (10^6 day· km^2) from 1978/79 to 2014/15, showing a slight negative trend (p not significant at 95%). (b) Melt extent (10^6 km^2) from 1978/79 to 2014/15, also showing a negative trend (p significant at 99%). A record low melt was observed during 2008/09. The year on the x-axis corresponds to the start of the austral summer melt season, e.g., 2008 corresponds to summer (DJF) 2008/09.

The melt index for the entire Antarctic continent has continued to drop since the 2012/13 season (Fig. 6.7a; Wang et al. 2014). The estimated melt index of the 2014/15 season is 29 252 500 day· km^2 in comparison to 39 093 125 day· km^2 in 2013/14 and 51 335 000 day· km^2 in the 2012/13 season. The melt extent of the 2014/15 season (Fig. 6.7b), however, is 1 058 750 km^2 , slightly greater than last year at 1 043 750 km^2 . The melt anomaly map in Fig. 6.6d shows the melt season was generally shorter than the historical average. Therefore, austral summer 2014/15 is classified as a low melt year for Antarctica. The 2014/15 melt extent and index numbers were almost equivalent to those observed during austral summer 2011/12 (944 375 km^2 and 29 006 250 day· km^2 , respectively). Figure 6.7 shows a nearly significant ($p = 0.05$) negative trend (311 900 day· km^2 yr $^{-1}$) in melt index and a significant ($p < 0.01$) negative trend (14 200 km^2 yr $^{-1}$) in melt extent over 1978/79 to 2014/15, highlighted by the record low melt season observed during austral summer 2008/09. The negative trends in melt index and melt extent are consistent with previous reports (Liu et al. 2006; Tedesco 2009a,b).

f. Sea ice extent, concentration, and duration—P. Reid, R. A. Massom, S. Stammerjohn, S. Barreira, J. L. Lieser, and T. Scambos

Net sea ice areal extent was well above average during the first few months of 2015 (Fig. 6.8a). Monthly record extents were observed in January (7.46×10^6 km^2), April (9.06×10^6 km^2), and May (12.1×10^6 km^2). The January extent marked the highest departure from average for any month since records began in 1979, at 2.39×10^6 km^2 above the 1981–2010 mean of 5.07×10^6 km^2 , or nearly 50% greater. These early season records follow on from the record high extent and late retreat of sea ice in 2014 (Reid et al. 2015). During the first half of 2015, there were 65 individual days of record daily sea ice extent, the last occurring on 11 July, and 46 record-breaking days of sea ice area within the first half of the year. However, the expansion of sea ice slowed so dramatically midyear that although sea ice area was at a record high level in May, it was at a record low level in August, just 83 days later (Fig. 6.8a). Close-to-average net sea ice extent levels were then observed in the latter half of 2015.

The record high net sea ice extent in January was dominated by strong positive regional anomalies in sea ice concentration and extent in the Ross and Weddell Seas (Figs. 6.8b, 6.9c,e) and across East Antarctica ($\sim 75^\circ$ – 140° E). This was counterbalanced by strong negative ice concentration and extent anomalies that were present in the Bellingshausen–Amundsen Seas (Figs. 6.8b, 6.9d). All three regions

of more extensive sea ice coincided with anomalously cool SSTs adjacent to the sea ice. Low atmospheric pressure anomalies were also present in the Weddell and Ross–Amundsen Seas (Fig. 6.3a). Interestingly, at this time colder-than-normal SSTs were present just to the north of the Bellingshausen–Amundsen Seas, possibly entrained within the ACC but not adjacent to the ice edge itself (and thus removed from the area experiencing below-normal ice extent).

As shown in Fig. 6.8a, there was a substantial and rapid decrease in the net ice extent (and area) anomaly from late January to early February, in large part due to changes in the eastern Ross (reflected in Fig. 6.9c) and western Amundsen (not shown) Seas. This rapid regional “collapse” followed lower-than-normal sea ice concentrations in the central pack ice during the latter part of 2014 (see Reid et al. 2015). In spite of this, net sea ice extent and area continued to track well above average or at record high levels between February and May. The Indian Ocean sector between ~60° and 110°E, the western Ross Sea, and the Weddell Sea showed particularly high or increasing sea ice concentrations during the February to May period as reflected in the regionwide daily anomaly series (Figs. 6.9a,c,e, respectively), with early-season areal expansion spurred on by colder-than-normal SSTs (not shown) and surface air temperatures (Figs. 6.3b,d).

June saw the beginning of a major change in the large-scale atmospheric pattern at higher southern latitudes, with lower-than-normal atmospheric pressure over the Antarctic continent and a strong atmospheric wave-3 pattern evolving (Fig. 6.3e). This coincided with warmer-than-normal SSTs in lower latitudes of the Indian and Pacific Oceans (the latter associated with the developing El Niño) and their influence on

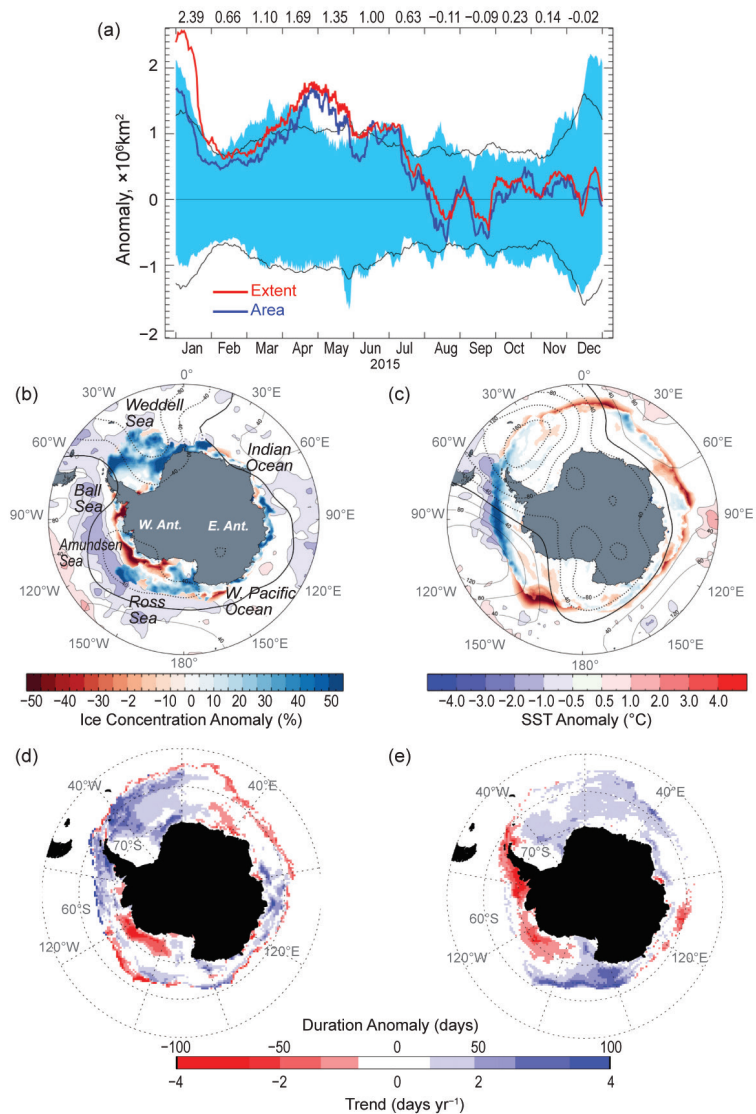


FIG. 6.8. (a) Plot of daily anomalies from the 1981–2010 mean of daily Southern Hemisphere sea ice extent (red line) and area (blue line) for 2015. Blue banding represents the range of daily values of extent for 1981–2010, while the thin black lines represent ± 2 standard deviations of extent. Numbers at the top are monthly mean extent anomalies ($\times 10^6 \text{ km}^2$). Sea ice concentration anomaly (%) maps for (b) Jan and (c) Sep 2015 relative to the monthly means for 1981–2010, along with monthly mean SST anomalies (Reynolds et al. 2002; Smith et al. 2008). These maps are also superimposed with monthly mean contours of 500-hPa geopotential height anomaly (Kalnay et al. 1996; NCEP). Bell is Bellingshausen Sea, AIS is Amery Ice Shelf. (d) Sea ice duration anomaly for 2015/16 and (e) duration trend (Stammerjohn et al. 2008). Both the climatology (for computing the anomaly) and trend are based on 1981/82 to 2010/11 data (Cavaliere et al. 1996, updated yearly), while the 2015/16 duration-year data are from the NASA Team NRTSI dataset (Maslanik and Stroeve 1999).

the distribution of atmospheric jets (Yuan 2004) and hence cyclonicity at higher southern latitudes. The abrupt change in hemispheric atmospheric circulation began a regional redistribution of patterns of sea ice areal expansion (Fig. 6.9). On one hand, there was

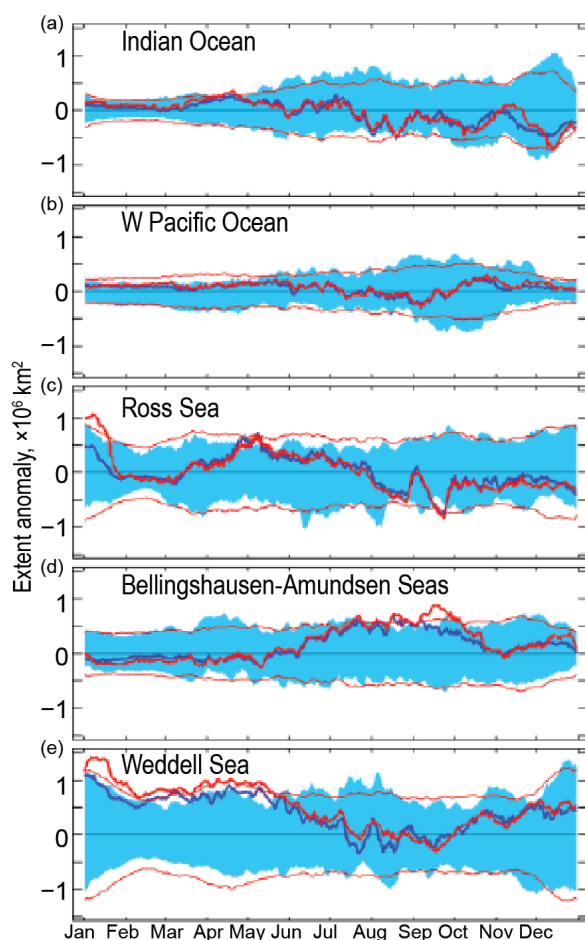


FIG. 6.9. Plots of daily anomalies ($\times 10^6 \text{ km}^2$) from the 1981–2010 mean of daily Southern Hemisphere sea ice extent (red line) and area (blue line) for 2015 for the sectors: (a) Indian Ocean; (b) western Pacific Ocean; (c) Ross Sea; (d) Bellingshausen–Amundsen Seas; and (e) Weddell Sea. The blue banding represents the range of daily values for 1981–2010 and the thin red line represents ± 2 std dev. Based on satellite passive-microwave ice concentration data (Cavalieri et al. 1996, updated yearly).

a reduction in the rate of expansion in the western Weddell and Ross Seas and much of East Antarctica ($\sim 30^\circ\text{E}$ – 180°). In other regions (i.e., the eastern Weddell and Ross Seas and Bellingshausen and Amundsen Seas), however, a likely combination of wind-driven ice advection and enhanced thermodynamics (colder-than-normal atmospheric temperatures, and in the Bellingshausen and Amundsen Seas region colder-than-normal SSTs) led to strongly positive sea ice extent anomalies. The anomalous ice extent patterns in the Ross Sea and Bellingshausen–Amundsen Seas were opposite to the trends observed over the last few decades of greater/lesser sea ice extent in those two regions respectively (Holland 2014). The net result of this redistribution in regional ice extent

anomalies was that net circumpolar sea ice extent and area dropped dramatically at the beginning of July (Fig. 6.8a). This general regional ice anomaly pattern then persisted to the end of September (Fig. 6.8c).

Another switch in large-scale regional sea ice extent anomalies occurred in October in response to the dissipation of the atmospheric wave-3 pattern and subsequent increase in negative pressure anomalies centered on $\sim 0^\circ$ and $\sim 170^\circ\text{W}$ and a broad ridge of positive pressure anomalies centered on $\sim 55^\circ\text{S}$, 90°W (Fig. 6.3g). Positive sea ice extent anomalies were associated with a combination of cold SSTs in the Bellingshausen–Amundsen Seas and cool atmospheric temperatures in the western Ross and Weddell Seas and far eastern East Antarctic. Negative anomalies were associated with relatively warm atmospheric temperatures to the east of the low pressure systems (Fig. 6.3h). At the same time, sea ice extent in the far eastern Weddell Sea and Indian Ocean sector ($\sim 0^\circ$ to $\sim 60^\circ\text{E}$) was well below average (Fig. 6.9a) and remained so for the rest of the year. This is attributable to the very low sea ice extent in the western Weddell Sea in the previous months (July–September as mentioned above), leading to lower-than-normal eastward advection of sea ice in the eastern limb of the Weddell Gyre (see Kimura and Wakatsuchi 2011). Similarly, a lack of eastward zonal advection of sea ice from the western Ross Sea resulted in lower-than-normal sea ice extent in the eastern Ross Sea ($\sim 150^\circ$ to $\sim 120^\circ\text{W}$). On a smaller scale, in late October through mid-November several intense low pressure systems caused a temporary expansion of the sea ice edge ($\sim 50\%$ above the long-term average) between $\sim 60^\circ$ and 90°E .

The net result of the seasonal sea ice anomalies described is summarized by the anomaly pattern in the annual ice season duration (Fig. 6.8d). The longer-than-normal annual ice season in the outer pack ice of the eastern Amundsen, Bellingshausen, and western Weddell Seas (120°W – 0°) was due both to an anomalously early autumn ice-edge advance and later spring ice-edge retreat. In contrast, the longer annual ice season in the inner pack ice zones of the western Weddell Sea and East Antarctic sector ($\sim 80^\circ$ – 120°E) was the result of anomalously high summer sea ice concentrations (Fig. 6.8b) that initiated an anomalously early autumn ice edge advance in those two regions. The shorter-than-normal annual ice season in the eastern Ross and western Amundsen Seas (160° – 120°W) was mostly due to an anomalously early ice edge retreat in spring associated with the increased negative pressure anomalies centered on 170°W and lack of zonal ice advection from the west. Though of lesser magnitude, similar spring factors

(the low pressure at 0° and lack of zonal ice advection from the west) were also implicated in the shorter-than-normal ice season in the far eastern Weddell Sea and western Indian Ocean sector between 10° and 40°E. The contrast in spring–summer anomaly patterns between the Bellingshausen–Amundsen Seas and eastern Ross Sea (Figs. 6.8c, 6.9c,d) is a somewhat typical response to El Niño and as such is opposite to the sea ice response to the atmospheric circulation pattern associated with a strong positive SAM index (and is also opposite to the long-term trend in annual ice season duration; Fig. 6.8e). However, and as described in Sidebar 6.1, the high-latitude response to this year’s El Niño was spatially muted relative to past El Niños due to the damping effect of the circulation anomalies associated with a mostly positive SAM index during this time.

g. Southern Ocean—J.-B. Sallée, M. Mazloff, M. P. Meredith, C. W. Hughes, S. Rintoul, R. Gomez, N. Metz, C. Lo Monaco, S. Schmidtko, M. M. Mata, A. Wählin, S. Swart, M. J. M. Williams, A. C. Naveria-Garabata, and P. Monteiro

The horizontal circulation of the Southern Ocean, which allows climate signals to propagate across the major ocean basins, is marked by eddies and the meandering fronts of the Antarctic Circumpolar Current (ACC). In 2015, large observed anomalies of sea surface height (SSH; Fig. 6.10a) contributed to variations in the horizontal ocean circulation. While many of these anomalies are typical of interannual variability, there were several regions where the 2015 anomaly was noteworthy due either to its extreme magnitude or its spatial coherence: north of the ACC in the Southwest Indian Ocean (~20°–90°E); in the entire South Pacific (~150°E–60°W), specifically the mid-Pacific basin around 120°W; and the anomalous negative SSH anomalies stretching around much of the Antarctic south of the ACC, especially over the Weddell Sea (0°–60°W). A large part of the 2015 SSH anomalies in the mid-Pacific, around Australia, and around South America was likely attributable to the strong El Niño event in 2015, though the low around Antarctica appears unrelated to ENSO variations (Sallée et al. 2008).

It is not straightforward to convert these large-scale SSH anomalies into anomalies of circumpolar volume transport. The best indicator of such variations is bottom pressure averaged on the Antarctic continental slope (Hughes et al. 2014), but such observations on the narrow slope regions are not available. Instead, the focus is on sea level averaged over this strip (Hogg et al. 2015). Figure 6.10d reveals that recent years have shown a resumption of the steady

rise in sea level in this region. A slight sea level fall in 2015 compared to 2014 remains consistent with this trend given the increase from 2014 to 2015 in eastward winds as represented by the SAM index (Fig. 6.10e), which is known to be associated with a fall in sea level (Aoki 2002; Hughes et al. 2003). A conversion from sea level to zonally averaged circumpolar transport, which is well established for periods of up to five years, is shown in Fig. 6.10e. This confirms the association with the atmospheric structures related to SAM but is suggestive of an additional source of variability associated with major El Niño (e.g., 2009/10, 2015/16) and La Niña (e.g., 1998/99, 1999/2000) events, when zonally averaged circumpolar transport anomalies became more negative (decreased transport) and positive (increased transport), respectively.

The horizontal circulation and vertical water-mass circulation are dynamically linked through a series of processes including surface water-mass transformation associated with air–sea–ice interactions. The characteristics of the lightest and densest of the Southern Ocean water masses are now described to provide an assessment of the vertical circulation and its contribution to ventilating the world’s oceans. The ocean surface mixed layer is the gateway for air–sea exchanges and provides a conduit for the sequestration of heat or carbon dioxide from the atmosphere into the ocean’s interior, which is ultimately mediated by the physical characteristics of the mixed layer.

The 2015 mixed layer temperature anomaly pattern revealed a distinct north–south dipole delimited by the ACC (Figs. 6.10b,c). Mixed layer conditions in Antarctic waters were very cold, whereas the mixed layers north of the ACC were warmer than average. This pattern persisted throughout both summer and winter, though with a reduced magnitude in winter. While the warm signal in the mid-Pacific was consistent with the influence of the 2015 El Niño event (Vivier et al. 2010), the cold signal south of the ACC was not. It was consistent, however, with the atmospheric circulation pattern associated with a positive SAM index that included increased northward Ekman transport of relatively cool and fresh Antarctic surface waters. In agreement, the southeast Pacific sector was fresher than the climatological average conditions, though other regions showed little homogeneity in salinity anomaly (not shown).

Mixed layer temperatures have a strong influence on air–sea CO₂ fluxes and ocean pH. Overall, the Southern Ocean is a net carbon sink. This sink decreased during the 1990s, but since 2002 has increased, reaching a maximum of about 1.3 Pg C yr⁻¹ in 2011 (Pg = 10¹⁵g; Landschutzer et al. 2015) and was

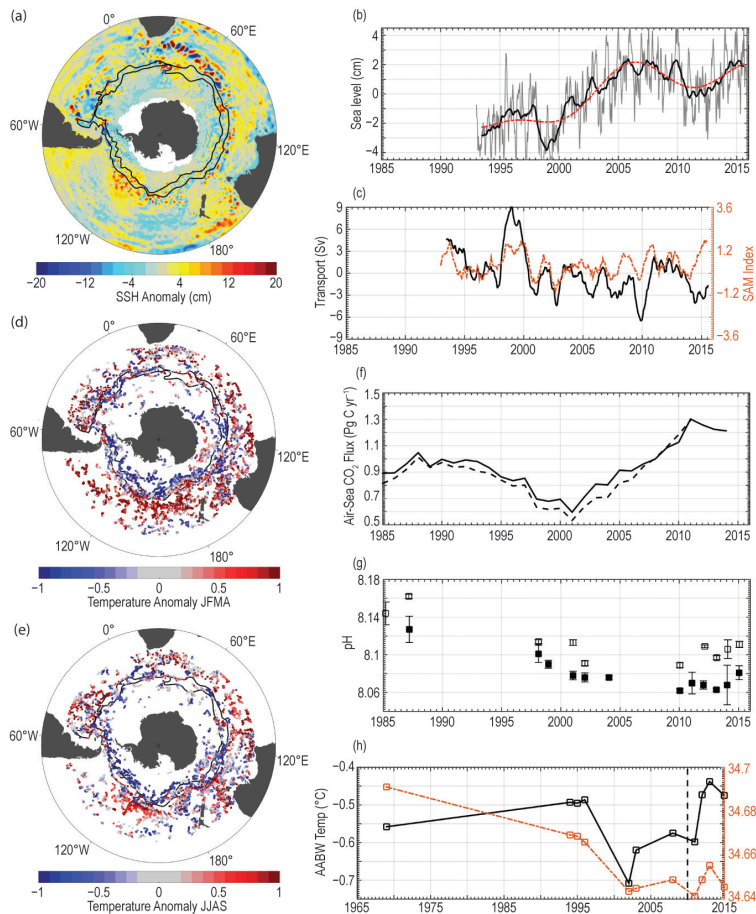


FIG. 6.10. (a) 2015 anomaly of sea surface height (cm) with respect to the 1993–2014 mean (produced from the Aviso SSH merged and gridded product). The trend at each location has been removed. (b) Time series (gray) of sea level anomaly (cm; produced from the Aviso SSH merged and gridded product) representative of a narrow region along the Antarctic coast (see Hogg et al. 2015) smoothed at different time scales. (c) Estimate of annual mean ACC transport anomaly (Sv, black line) derived from sea level (Hogg et al. 2015) with SAM index (Marshall et al. 2003) superimposed (dashed orange line). (d) 2015 anomaly of mixed layer temperature ($^{\circ}\text{C}$) in summer (Jan–Apr) with respect to the climatological mean (2000–2014; computed from all available Argo observations). (e) Same as (d) but for the winter anomaly (Jul–Sep). In (a, d, e), the two black lines represent the mean location of the two main fronts of the ACC (Orsi et al. 1995). (f) Evolution of the Southern Ocean carbon sink (Pg C yr^{-1}) south of 35°S , showing the flux derived from an interpolation method (Landschutzer et al. 2015) based on surface ocean $p\text{CO}_2$ data from SOCAT-V3 (black solid line) and from SOCAT-V2 (black dotted line; Bakker et al. 2014). Positive values refer to a flux from air to ocean (i.e., ocean acts as a sink). (g) Evolution of pH in the Antarctic surface water (around 56°S , solid square) and subantarctic surface water (around 40°S , hollow square) in the South Indian Ocean; only repeat summer stations are used. (h) Potential temperature ($^{\circ}\text{C}$, black line) and salinity (dashed orange line) of Antarctic Bottom Water at 140°E for 1969–2015; only repeat summer stations are used. Potential temperature and salinity are averaged over the deepest 100 m of the water column for stations between 63.2° and 64.4°S , in the core of the AABW over the lower continental slope (average pressure of 3690 dbar). The vertical dashed line indicates the date of the calving of the Mertz Glacier Tongue. Note that time axis in (h) is different from (b), (c), (f), and (g).

likely stronger than 1 Pg C yr^{-1} in 2015 (Fig. 6.10f). South of the ACC, the increase of the sink is explained by the cooling of the surface layer in summer (Fig. 6.10b) and the stability of the CO_2 concentrations in winter (Munro et al. 2015). The ocean carbon uptake leads to a decrease in pH, the so-called ocean acidification. A global assessment of surface water pH in 2015 is not possible due to scarcity of observations, so we present the evolution of pH in the South Indian sector, which has been monitored since 1985 (Fig. 6.10g). A rapid pH change was identified in 1985–2001 ($-0.03 \text{ decade}^{-1}$) but has stabilized since 2002 (Fig. 6.10g), a signal probably associated with a shift in climate forcing (e.g., neutral state of SAM in 2000s; Fig. 6.10e).

The bottom layers of the Southern Ocean are also undergoing substantial changes. Linear trends of deep ocean change constructed from repeat sections between 1992 and 2005 reveal abyssal warming, with the strongest warming close to Antarctica (Purkey and Johnson 2010; Talley et al. 2016). Antarctic Bottom Water (AABW) is also contracting in volume and freshening (Purkey and Johnson 2012, 2013; Shimada et al. 2012; Jullion et al. 2013; van Wijk and Rintoul 2014; Katsumata et al. 2014; Meredith et al. 2014). These changes reflect the response of AABW source regions to changes in surface climate and ocean–ice shelf interaction and to downstream propagation of the signal by wave and advective processes (Jacobs and Giulivi 2010; van Wijk and Rintoul 2014; Johnson et al. 2014).

As with pH, observations of the deep ocean remain scarce, preventing a global assessment of the state of the abyssal ocean in 2015. However, repeat occupa-

tions of hydrographic sections at 140°E provide a record of variations in AABW properties immediately downstream of a primary source of bottom water (Fig. 6.10h). Potential temperature shows significant variability but no long-term trend between 1969 and 2015. In contrast, the long-term trend in salinity (~ -0.01 decade $^{-1}$; Fig. 6.10h) exceeds interannual variability. Calving of the Mertz Glacier Tongue in 2010 reduced the area of the Mertz polynya and thereby reduced the amount of sea ice and dense water formed in the polynya (Tamura et al. 2012; Shadwick et al. 2013), which likely contributed to the AABW variations observed after 2010.

h. Antarctic ozone hole—E. R. Nash, S. E. Strahan, N. Kramarova, C. S. Long, M. C. Pitts, P. A. Newman, B. Johnson, M. L. Santee, I. Petropavlovskikh, and G. O. Braathen

The 2015 Antarctic ozone hole was among the largest and most persistent ever observed, based upon the record of ground and satellite measurements starting in the 1970s. Figure 6.11a displays the daily areal coverage of the Antarctic ozone hole during 2015 (blue line) compared to the 1986–2014 climatology (white line). The ozone hole area is defined as the area covered by total column ozone values less than 220 Dobson Units (DU). For 2015, area values greater than 5 million km² first appeared in late August, ap-

proximately two weeks later than typical. The ozone hole usually reaches its largest size by mid-September, but in 2015 the maximum size occurred on 2 October at 28.2 million km². The ozone hole then persisted at this large size (>20 million km²) until 15 November, setting daily records during much of October and November. The development of ozone depletion over time (daily minimum values; Fig. 6.11b) indicates that the ozone minimum was reached near 2 October; ozone then remained near record low values until early December. The late start, persistent large area, and low ozone minima were caused by unusually weak stratospheric wave dynamics.

NOAA ozonesondes are launched regularly over South Pole station. In early October 2015, the 12–20-km column ozone was close to the long-term mean (Fig. 6.12a), while ozone increases thereafter were delayed compared to the long-term record. The minimum 12–20-km column ozone in 2015 was the fourth lowest at 7.2 DU, measured on 21 October (ozone hole image Fig. 6.11a). The ozonesonde total column minimum was 112 DU on 15 October. The ozonesonde of 8 December 2015 (ozone hole image Fig. 6.11b) showed record low total column ozone for early December, highlighting the abnormally late breakup of the hole.

One of the key factors controlling the severity of the Antarctic ozone hole is stratospheric temperature. Lower temperatures allow more polar stratospheric cloud (PSC) formation, exacerbating ozone depletion. Southern Hemisphere stratospheric dynamical conditions were anomalous in spring 2015. The lower stratospheric polar cap temperatures from the NCEP–DOE Reanalysis 2 for 2015 (Fig. 6.12b, blue line) were near the climatological average through August, but were below climatology during September–November.

The 100-hPa eddy heat flux is a measure of wave propagation into the stratosphere. A smaller (larger) magnitude leads to colder- (warmer-) than-average temperatures. The heat flux was generally below average for July–October (Fig. 6.12c), especially in October. As a result, temperatures warmed at a slower rate in September–October (Fig. 6.12b), and the vortex eroded more slowly than in previous years. Consequently, the ozone hole was persistent, and stratospheric ozone levels at South Pole remained below average during October–November (Fig. 6.12a).

The 2015 ozone hole broke up on 21 December, about two weeks later than average. The breakup is identified as the date when total ozone values below 220 DU disappear (see Fig. 6.11). Ozone hole breakup is tightly correlated with the stratospheric polar vor-

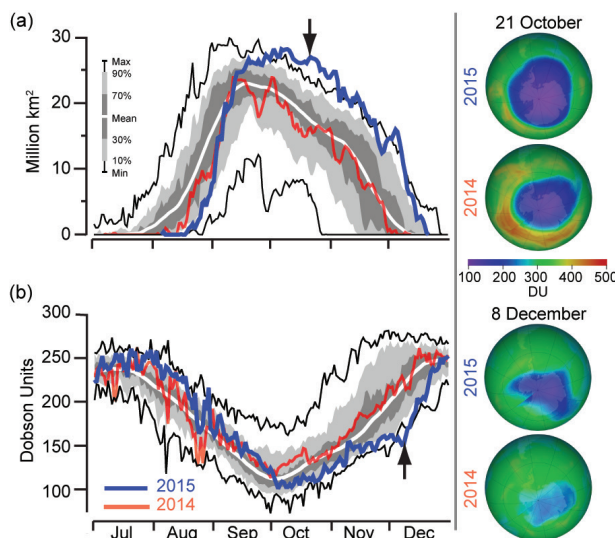


FIG. 6.11. (a) Area coverage of the Antarctic ozone hole as defined by total column ozone values less than 220 DU and (b) daily total column ozone minimum values in the Antarctic region from TOMS/OMI for 2014 (red line) and 2015 (blue line). The average of the daily values (thick white line), the record maximum and minimum sizes (thin black lines), and the percentiles (gray regions and legend in a) are based on a climatology from 1986–2014. The black arrows indicate the dates of the ozone maps on the right side.

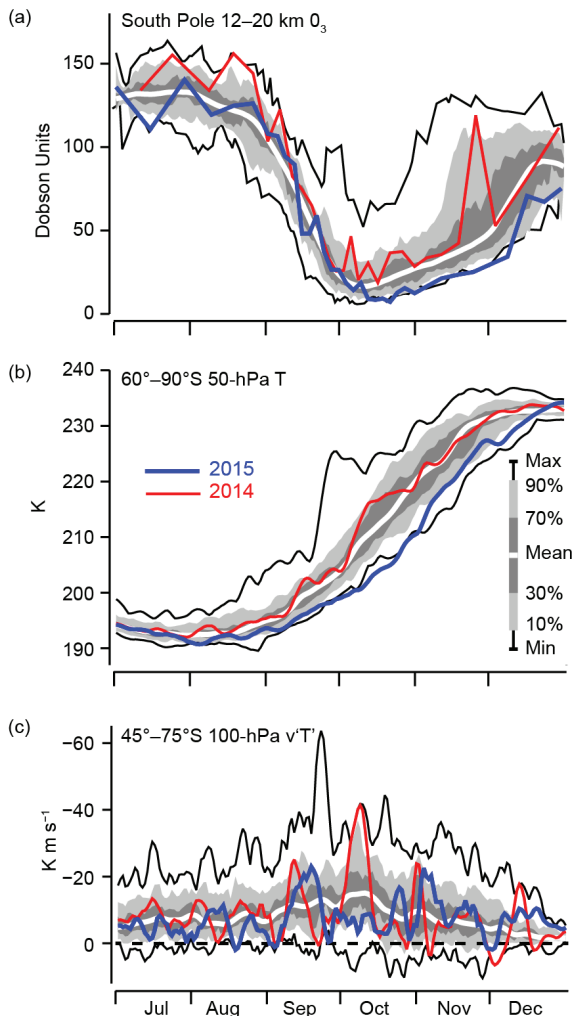


FIG. 6.12. (a) Column ozone from NOAA South Pole ozonesondes measured over the 12–20-km (~160–40-hPa) range. (b) NCEP–DOE Reanalysis 2 of lower stratospheric temperature (60°–90°S, 50-hPa). (c) NCEP–DOE Reanalysis 2 of zonal mean eddy heat flux (45°–75°S, 100 hPa). The blue lines show the 2015 values and the red lines show 2014. The average of the daily values (thick white line), the record maximum and minimum sizes (thin black lines), and the percentiles [(gray regions and legend in (b))] are based on a climatology from (a) 1986–2014 and (b), (c) 1979–2014.

tex breakup, which is driven by wave events propagating upward into the stratosphere, thus enabling transport of ozone-rich air from midlatitudes. The 2015 ozone hole broke up late because of weak wave driving in October–November (Fig. 6.12c).

Levels of chlorine and bromine continue to decline in the stratosphere, and improvement of ozone conditions over Antarctica is expected. Ozone depletion is estimated using equivalent effective stratospheric chlorine (EESC)—a combination of inorganic chlorine (Cl_y) and bromine. Using a mean age of air of 5.2

years, EESC shows a 2000–02 peak of 3.8 ppb, with a projected decrease in 2015 of 9% to 3.45 ppb as a result of the Montreal Protocol. This is a 20% drop towards the 1980 (“pre-ozone hole”) level of 2.03 ppb. NASA *Aura* satellite Microwave Limb Sounder (MLS) N_2O measurements can be used to estimate Antarctic stratospheric Cl_y levels (Strahan et al. 2014). Antarctic EESC has a small annual decrease (<1% yr^{-1}), but interannual variations in transport to the Antarctic vortex cause Cl_y to vary by up to $\pm 8\%$ with respect to expected levels. Similar to 2014, the 2015 Antarctic stratospheric Cl_y was higher than recent years and similar to levels found in 2008 and 2010.

MLS lower stratospheric chlorine and ozone observations in the vortex were consistent with the

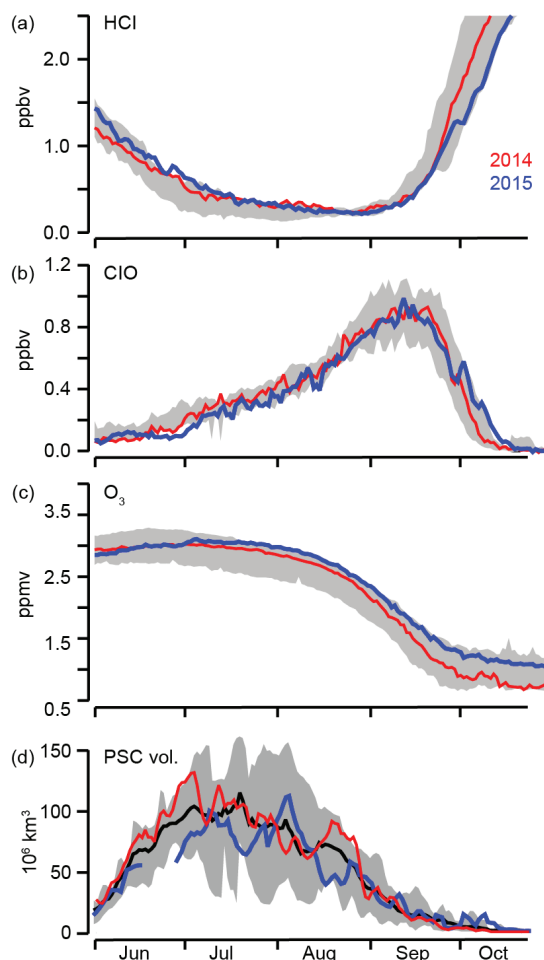


FIG. 6.13. Time series of 2014 (red line) and 2015 (blue line) Antarctic vortex-averaged: (a) HCl, (b) ClO, and (c) ozone from *Aura* MLS (updated from Manney et al. 2011). These MLS averages are made inside the polar vortex on the 440-K isentropic surface (~18 km or 65 hPa). The gray shading shows the range of Antarctic values for 2004–14. (d) Time series of 2014 (red line) and 2015 (blue line) CALIPSO PSC volume (updated from Pitts et al. 2009). The gray shading shows the range for 2006–14, and the black line is the average.

SIDEBAR 6.2: POLAR ECOSYSTEMS AND THEIR SENSITIVITY TO CLIMATE PERTURBATION—H. DUCKLOW AND A. FOUNTAIN

Ice exerts a dominant control on the function and structure of polar ecosystems. Depending on the organism, it provides habitat and foraging platforms, or serves as a barrier to food and the flow of nutrients (Fountain et al. 2012). Polar ecosystems, both terrestrial and marine, have evolved and adapted to pervasive ice conditions, so when air temperatures rise above the melting threshold, the normal balance of water and ice shifts dramatically, resulting in a series of cascading effects that propagate through the entire ecosystem. The effects may persist for years to decades (J. Prisco 2016, manuscript submitted to *BioScience*).

In Antarctica, the differences between marine and terrestrial ecosystems could not be more extreme. These two biomes are the focus of two NSF-funded Long Term Ecological Research (LTER) programs: the Palmer LTER (or PAL), which is studying the rapidly changing marine ecosystem west of the Antarctic Peninsula (Ducklow et al. 2013), and the McMurdo Dry Valleys LTER (or MCM), which is studying the terrestrial ecosystem in the Dry Valley polar desert (Freckman and Virginia 1997). Established in the early 1990s, these two Antarctic sites collect baseline measurements to develop process-level understanding, thus providing necessary context for evaluating ecological responses to climate events.

The marine ecosystem surrounding Antarctica includes the coastal and continental shelf region that is influenced by seasonal sea ice cover, as well as the permanently open ocean zone poleward of the Antarctic Circumpolar Current (Treguer and Jacques 1992). Primary production in these regions is dominantly by phytoplankton. Although considerable regional and seasonal variability exists, Antarctic food webs are typically supported by diatoms with variable contributions by other types of phytoplankton. Diatom-based food webs are typically characterized by highly variable but sometimes vast swarms of Antarctic krill. Krill in turn are the principal food for the conspicuous large predators of Antarctic seas, including penguins and other seabirds, seals, and whales (Hardy 1967).

This general picture has served as the paradigm for the Antarctic marine ecosystem for decades, but it appears to be changing, at least in the rapidly warming (Smith et al. 1996) western Antarctic Peninsula region (WAP) of the Bellingshausen Sea. Ecological change along the WAP was first marked by catastrophic declines in Adélie penguins (Fig. SB6.2a; Fraser and Hofmann 2003; Bestelmeyer et al. 2011). The principal cause of ecological change is decreasing sea ice cover in the WAP and greater Bellingshausen Sea—both its extent and duration (Fig. 6.8e; Stammerjohn

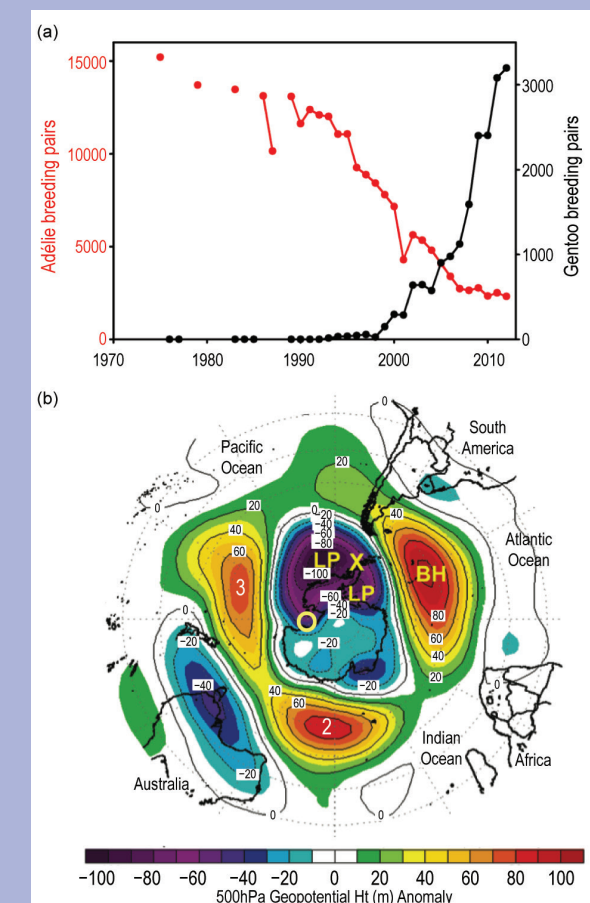


FIG. SB6.2. (a) The number of breeding pairs of Adélie and Gentoo penguins near Palmer Station, 1976–2013. The Gentoo is a subpolar, ice-tolerant invasive species that has colonized the polar region as sea ice cover has declined and water temperatures have increased. The first Gentoo pairs were observed at this location in 1994. (b) Monthly mean composite anomaly map of 500-hPa geopotential height centered over Antarctica for Sep 2001 to Feb 2002 relative to the mean calculated over Sep to Feb 1980–2001. BH and LP denote blocking high pressure and low-pressure anomalies, respectively. The yellow X is close to Palmer Station and the yellow circle is close to McMurdo Station. (From Massom et al. 2006.)

et al. 2012). Diatom blooms, krill recruitment, and penguin breeding success are all dependent on the extent of sea ice and the timing of its retreat (Saba et al. 2014; Montes-Hugo et al. 2009). Other changes in the freshwater system are also known to influence the marine ecosystem. Glacial discharge and melt, for example, have the capacity to increase ocean stratification and add bio-available micronutrients, such as iron, to the productive upper

layers (Boyd and Ellwood 2010; Hawkings et al. 2014). Changes in any of these environment variables can lead to functionally extinct species and a reorganization of the marine ecosystem (e.g., Saillely et al. 2013).

Antarctic terrestrial ecosystems, at least those that inhabit the largest ice-free areas of the Antarctic continent, the Dry Valleys (78°S, 162°E), exist in a landscape that includes glaciers, perennially ice-covered lakes, seasonal meltwater streams, and arid soils (Ugolini and Bockheim 2008). No vascular plants or vertebrates inhabit the region, and food webs are dominated by bacteria, cyanobacteria, fungi, yeasts, protozoa, and a few taxa of metazoan invertebrates (Freckman and Virginia 1997). Glacial meltwater is the primary source of water, which flows in ephemeral streams and conveys water, solutes, sediment, and organic matter to the lakes (Fountain et al. 1998; McKnight et al. 1999). Streams flow for up to 12 weeks in the austral summer providing a habitat for microbial mats abundant in streambeds stabilized by stone pavement (McKnight et al. 1998). Perennial water environments include ice-covered lakes in the Dry Valleys of Antarctica; they maintain biological activity year-round with food webs dominated by phytoplankton and bacteria (Laybourn-Parry 1997).

The two LTER sites are separated by about 3800 km (Fig. 6.1). On annual time scales, air temperatures at these two sites are inversely related (A. Fountain et al. 2016, manuscript submitted to *BioScience*; M. Obryk et al. 2016, manuscript submitted to *BioScience*) due mostly to the circulation anomalies associated with the SAM index (Trenberth et al. 2007). On decadal time scales, the lower-latitude PAL site is also experiencing rising air temperatures (+3°C increase in annual temperatures over 1958–2014), while the higher-latitude MCM site is experiencing a more modest change [+1°C over the same time period; A. Fountain et al. (2016), manuscript submitted to *BioScience*].

However, in the austral spring/summer of 2001/02, a hemisphere-wide atmospheric circulation anomaly caused

unusually high temperatures across the entire continent (Fig. SB6.2b; Massom et al. 2006), which had long-lasting impacts.

At MCM, the rapid melting of glacial ice caused streams to flow at record levels, eroding stream banks and rapidly raising lake levels (Foreman et al. 2004). The stream waters transported unusually high concentrations of sediments and nutrients to the ice-covered lakes. Phytoplankton chlorophyll-*a* concentrations reached record high levels that austral summer but also remained at elevated levels for almost a decade. Elevated soil moisture caused a reorganization of species composition in the soils that was still evident seven years later (Barrett et al. 2008).

At PAL, warm, moist northwesterly winds caused a rapid and early ice edge retreat in early spring (September–October 2001) that subsequently compacted and piled the ice against the Peninsula. Snowfall was also anomalously high during this time (Massom et al. 2006). Abundances of krill species were higher than normal, likely due to the high productivity associated with the compacted sea ice inshore (Steinberg et al. 2015). The positive chlorophyll-*a* anomaly in 2001/02 corresponded to a statistically significant krill recruitment event (evidenced in Adélie penguin diet samples) the following year (Saba et al. 2014). However, it was the catastrophic late-season snowfalls and subsequent flooding that caused the largest single-season decline in Adélie penguin breeding success in 30 years (Fraser et al. 2013). There was a devastating loss of an entire breeding cohort, an effect that is still evident 10 years later.

The climate event of 2001/02 illustrates the extreme sensitivity of polar ecosystems and also illustrates how an anomalous event can induce connectivity across different regional climates. As exemplified here, a relatively small but critical change in the temporal and spatial distributions of ice and water exhibited dramatic and persistent ecological responses, the implications of which are still being studied.

late start of the 2015 ozone hole (Fig. 6.11a). The reformation of hydrogen chloride (HCl; Fig. 6.13a) and decrease of chlorine monoxide (ClO; Fig. 6.13b) occurred late in 2015. The 440-K potential temperature ozone levels (Fig. 6.13c) were higher than average in July–September, but declined to very low values by mid-October, consistent with Fig. 6.12a.

Heterogeneous chemical reactions on PSC surfaces convert reservoir chlorine (e.g., HCl) into reactive

forms (e.g., ClO) for catalytic ozone loss. The PSC volume (Fig. 6.13d), as measured by the *Cloud-Aerosol Lidar and Infrared Pathfinder Satellite Observation (CALIPSO)*, generally followed the average (black line) for the entire season. However, the October 2015 volume of 5.6 million km³ ranked highest of all 10 years, consistent with the persistent and large October ozone hole (Fig. 6.11a).

Satellite column observations over Antarctica (not shown) show some indications that ozone loss

has diminished since the late-1990s. Averaged daily minima over 21 September–16 October (ozone hole maximum period) have increased since 1998 at a rate of 1.2 DU yr^{-1} (90% confidence level). The 2015 ozone hole area, averaged over 7 September–13 October, was estimated at 25.6 million km^2 , the fourth largest over the 1979–2015 record. Since 1998, this area is decreasing at a rate of $-0.09 \text{ million km}^2 \text{ yr}^{-1}$, but this trend is not statistically significant. The decline of chlorine concentrations should eventually

be manifested in smaller and shallower Antarctic ozone holes. However, unambiguous attribution of the ozone hole improvement to the Montreal Protocol cannot yet be made because of relatively large year-to-year transport, wave activity, temperature variability, and observational uncertainty. Further information on the ozone hole, with data from satellites, ground instruments, and balloon instruments, can be found at www.wmo.int/pages/prog/arep/gaw/ozone/index.html.